Modulation of Spindle Assembly Checkpoint efficiency by cell fate in a chordate embryo

Short title: The SAC in chordate embryos

Marianne Roca[1,2], Lydia Besnardeau[1], Elisabeth Christians[1], Alex McDougall[1], Janet Chenevert[1*], Stefania Castagnetti[1*]

[1] Sorbonne Universités, CNRS, Laboratoire de Biologie du Développement de Villefranche-sur-Mer (LBDV), 06230 Villefranche-sur-Mer, France.

[2] current address: Max Planck Research Group Genetics of Behavior, Max Planck Institute for Neurobiology of Behavior – Caesar, Ludwig-Erhard-Allee 2, Bonn 53175, Germany

* corresponding authors: stefania.castagnetti@imev-mer.fr

Keyword: mitosis, ascidian, spindle assembly checkpoint, embryo, kinetochore, chordate

Abstract

The spindle assembly checkpoint (SAC) is a surveillance system which preserves genome integrity by delaying anaphase onset until all kinetochores are correctly attached to spindle microtubules. Recruitment of SAC proteins to unattached kinetochores generates an inhibitory signal that prolongs mitotic duration. Chordate embryos are atypical in that spindle defects delay mitotic progression only during late embryogenesis and it is not known whether once acquired the SAC is then under the same regulation as in non-chordate embryos. Here we show that in embryos of the chordate *Phallusia mammillata* the SAC is inefficient during the first seven cleavage divisions. From the 8th cell cycle, the SAC becomes able to delay mitotic exit in all cells but its strength, manifest as the degree of mitotic lengthening induced by spindle perturbations, is specific to different cell types and is modulated by cell size showing similarity to SAC control in the early cell cycles of *Caenorhabditis elegans*. The difference in SAC strength requires GSK3 kinase activity. We suggest that in chordates modulation of SAC efficiency in SAC proficient stages depends on cell fate and cell size similarly to the early cell cycles of non-chordate embryos.

Introduction

The spindle assembly checkpoint (SAC), or mitotic checkpoint, is a control mechanism that operates during mitosis to ensure fidelity of chromosome segregation, by delaying anaphase onset until all chromosomes have acquired proper bipolar attachments to spindle microtubules. Loss of SAC function is often associeted with chromosome segregation errors which result in the generation of daughter cells with an abnormal chromosome number, a condition called aneuploidy, deleterious for cell viability and organismal survival (Chunduri and Storchová, 2019; Jia et al., 2013; Musacchio and Salmon, 2007).

Although the SAC has an essential role to ensure genomic stability, the response to spindle defects varies across cell types, from the absence of SAC response in early chordate embryos to the permanent mitotic arrest of HeLa cells. Studies carried out in *Caenorhabditis elegans* embryos have attributed this variability to differences in cell size and cell identity. In those embryos the SAC becomes more efficient, delaying mitosis for longer, at each cleavage division following fertilization, as cell volume is reduced (Encalada et al., 2005; Galli and Morgan, 2016; Gerhold et al., 2018). These data can be explained by a model whereby SAC signal generated at kinetochores is diluted in the cytoplasm and the strength of SAC response is influenced by kinetochore-to-cytoplasmic ratio. Consistent with this notion, in *Xenopus* egg extracts, the mitotic checkpoint can be activated by increasing the concentration of added sperm heads(Minshull et al., 1994) and in mouse reduction of oocyte size results in a stronger SAC response during meiosis (Kyogoku and Kitajima, 2017; Lane et al., 2017). However, recent work indicated that cell size does not influence SAC strength in mouse pre-implantation embryos (Vázquez-Diez et al., 2019). Similarly, in *C. elegans* embryos, the germline lineage displays a stronger checkpoint response than somatic cells and this difference cannot be accounted for by a difference in cell size, but was shown to depend on the partitioning of cell fate determinants (Gerhold et al., 2018).

Here we find that in the chordate *P. mammillata* the SAC becomes efficient at the 8th cell cycle and its strength then increases at each cell division. We show that, following SAC acquisition SAC strength is influenced by cell identity, similarly to SAC proficient non-chordate embryos (Gerhold et al., 2018) and we suggest that within same-fated cells SAC strength is then modulated by changes in cell size. In the ventral ectoderm of *P. mammillata* embryos, the difference in SAC activity observed between anterior and posterior cells requires GSK3 activity to enhance SAC strength in anterior cells.

68 **Results and Discussion**

69 We have previously shown that the SAC is inefficient in 2-cell stage embryos of *P.*
70 *mammillata* where treatment with nocodazole completely depolymerizes microtubules,
71 preventing spindle formation, but induces only a limited mitotic delay (Chenevert et al., 2020).
72 As an active SAC delays mitotic exit, to determine when the SAC becomes functional in *P.*
73 *mammillata* embryos, we analyzed mitotic duration in the absence of spindle microtubules (Fig
74 S1), from the 2nd to 10th cell cycle following fertilization. Mitotic duration was measured as the
75 time spent between nuclear envelope breakdown (NEB), and nuclear envelope reformation
76 (NER; Fig 1A). Consistent with earlier studies (Dumollard et al., 2017), mitotic duration in
77 control embryos (DMSO) was constant at all analyzed stages (Fig 1B) and lasted on average
78 10 minutes. As previously observed for 2-cell stage embryos (Chenevert et al., 2020), mitotic
79 duration was briefly delayed in 2- to 64-cell stage embryos treated with nocodazole, compared
80 to DMSO-treated embryos (1.5-fold) (Fig 1B). From the 8th cell cycle, however, in nocodazole-
81 treated embryos mitotic duration was prolonged more extensively at each cell cycle, extending
82 by 2.5-fold (24.5±8.5 minutes) at the 8th cell cycle (128 cell), by 4.5-fold (37.3±14.5 minutes)
83 at the 9th cell cycle (256-cells) and by 6.5-fold (64.3±20 minutes) at the 10th cell cycle (512-
84 cells). These results suggest that the SAC becomes efficient at the 8th cell cycle and that its
85 efficiency increases progressively in the following cell cycles.

86 To confirm that the mitotic delay observed from the 8th cell cycle requires SAC activity,
87 we measured mitotic duration in the presence of nocodazole in SAC impaired embryos (Fig
88 2A). Mutations of three phosphorylation sites in the human SAC protein Mad2 produce a
89 dominant negative form of Mad2 (Mad2-DN) that impairs SAC activity (Fig 2B) (Wassmann
90 et al., 2003a; Wassmann et al., 2003b). We tested the effect of Mad2-DN on mitotic duration
91 during *P. mammillata* development. At the 2-cell stage, overexpression of Mad2-DN did not
92 affect mitotic duration, either in the presence (Fig 2C) or in the absence (Fig 2D) of
93 microtubules. However, both at the 8th and the 9th cell cycles mitotic duration in the presence of
94 nocodazole was significantly reduced by Mad2-DN overexpression (Fig 2D) lasting only 1.5
95 times longer in nocodazole-treated than in DMSO-treated embryos (128-cell: DMSO = 9.8±1.6
96 to nocodazole = 15.6±3.5 minutes; 256-cell: 9.9±1.8 to 13.6±2.4 minutes), comparable to
97 mitotic duration in nocodazole treated wild-type early embryos (2- to 64- cell stage). Similarly
98 impairing SAC activity with reversine, a specific inhibitor of Mps1, the kinase that initiates the
99 SAC signaling cascade (Fig 2A)(Santaguida et al., 2010), prevents mitotic lengthening
100 following nocodazole treatment at the 9th cell cycle (Fig 2D). Hence, the SAC is required to

101 delay mitotic exit from the 8th cell cycle but does not control mitotic progression during the
102 previous seven divisions.

103 After the 8th cell cycle, SAC response increases both in strength and variability at each
104 cell cycle (Fig. 1B). At this stage, most cells in the ascidian embryo are fate-restricted. We then
105 asked whether SAC strength is a property of different cell identities and therefore analyzed
106 SAC strength in different cell populations. We observed that at the 9th cell cycle, in the presence
107 of nocodazole, cells of the anterior ventral ectoderm spent significantly longer in mitosis than
108 cells of the posterior ventral ectoderm, dorsal ectoderm or notochord (Fig. 3A, B).

109 To dissect which factors influence this difference in SAC strength we focused on the
110 ventral ectoderm as those cells are easily accessible, being on the surface of the embryo, and
111 two SAC behaviors can be observed in the same field of view. We first asked whether the
112 difference between these two populations could be explained by a difference in cell size. Using
113 the membrane marker PH-GFP, we measured cell volume and observed that ventral anterior
114 and posterior ectodermal cells have a similar range of cell volumes (Fig. 3C), excluding that
115 the difference in mitotic response between these two cell populations is due to a difference in
116 cell size.

117 We then asked whether the difference in SAC strength observed in the ventral ectoderm
118 along the antero-posterior axis is a consequence of the differences in cell fate. We therefore
119 interfered with patterning along the anterior-posterior axis and analyzed SAC strength at the 9th
120 cell cycle. In *C. intestinalis* the transcription factor FoxA-a is necessary for the acquisition of
121 anterior ectodermal identity and its overexpression in animal blastomeres from the 16-cell stage
122 results in posterior cells acquiring anterior identity (Lamy et al., 2006). To induce anterior fate
123 in the posterior part of the ventral ectoderm we injected *P. mammillata* eggs with a plasmid
124 encoding FoxA-a under the control of the Fog promoter (pFog>FoxA-a) to drive FoxA-a
125 expression in all animal cells. At the 9th cell cycle, in pFog>FoxA-a injected embryos expression
126 of the anterior marker sFRP1/5 (Lamy et al., 2006), normally restricted to the anterior pole (Fig
127 S2A), was extended towards the posterior pole in 34% of embryos and was expressed in all
128 cells in 66% of embryos. The latter did not elongate at the neurula stage but developed into
129 round embryos, indicating complete loss of anterior-posterior patterning. At the 9th cell cycle,
130 mitotic duration was unaffected in pFog>FoxA-a-injected embryos in the presence of DMSO
131 (Fig S2B). In nocodazole-treated round pFog>FoxA-a-injected embryos (Fig 3D) mitotic
132 duration was extended by 4.4-fold (11.1±2.6 to 48±21.7 minutes), an increase similar to that
133 observed in anterior wild-type cells (9.9±2.4 to 49.3±11.9 minutes, 4.8-fold increase). To
134 confirm that anteriorization of the posterior ectoderm results in an increase in SAC strength,

we also removed the vegetal pole of fertilized eggs, which contains the maternal factors required for cell differentiation and for the invariant cleavage pattern typical of ascidian development (Fig. 3E)(Nishida, 1996; Nishikata et al., 1999). Such manipulation of the zygote (pole-ablated) gives rise to embryos in which all cells acquire the anterior ectodermal fate (Nishida, 1994), as shown by ectopic expression of the anterior marker sFRP1/5 (Lamy et al., 2006) throughout the embryo (Fig. S2A). Pole-ablated embryos acquire SAC activity at the 8th cell cycle and in the presence of nocodazole delay mitotic duration by 2.4-fold (DMSO: 10.7±2.9 to nocodazole: 24.3±7.5 minutes), like ventral anterior ectodermal cells in control, un-manipulated embryos (Fig. S2C). At the 9th cell cycle, we observed greater variability in mitotic duration in pole-ablated embryos than in anterior ectodermal cells of wild-type embryos, with several cells exhibiting only a short mitotic delay (Fig. 3F). However, we noticed that differently from unmanipulated control embryos where the cell volume of anterior ectodermal cells ranges between $2x10^3$ μm^3 and $4x10^3$ μm^3, in pole-ablated embryos cell volume varied between, $1.8x10^3$ μm^3 and $8x10^3$ μm^3 (Fig. 3G). The mitotic delay induced by nocodazole was comparable in control (48±11.9 minutes) and pole ablated (43.5±15.6 minutes) embryos when considering only cells whose volume was comparable to anterior ectodermal cells (volume<$4x10^3$ μm^3), while in pole ablated cells larger than $4x10^3 \mu m^3$ the mitotic delay was significantly shorter (25.3±6.9 minutes, 2.2-fold increase, Fig 3G and Fig S2D). Hence, the difference in SAC efficiency between anterior and posterior ectodermal cells could be attributed to a difference in cell identity. Our data also suggest that within same fated cells, the SAC response is modulated by cell size and is stronger in smaller cells. However, given the asynchrony in cell division from the 4th cell cycle in *P. mammillata* embryos, it is formally possible that SAC strength increases at each cell division cycle and larger cells have a weaker SAC because they are a cell cycle behind due to cell cycle asynchrony.

As anteriorization of posterior cells results in enhancement of SAC strength we then asked whether posteriorization of the anterior ectoderm would result in a reduction in SAC efficiency. In the ascidian *Ciona intestinalis*, GSK3 is active in anterior cells and its inhibition from the onset of gastrulation results in loss of anterior identity in the ectoderm with extension of the posterior domain (Feinberg et al., 2019). We observed a similar effect in *P. mammillata* embryos treated with the specific GSK3 inhibitor BIO from the onset of gastrulation (stage 10, Fig. 4A). BIO-treated embryos did not express the anterior markers FoxF (Fig. 4B) and sFRP1/5 (Fig S2E), and developed into tadpoles with diminished anterior structures (Fig. 4B)(Feinberg et al., 2019), consistent with the acquisition of posterior identity in the anterior ventral ectoderm. At the 256-cell stage, BIO-treated embryos maintained their overall shape, allowing

169 orientation of the embryo along the anterior-posterior axis (Fig. 4B). At this stage, mitotic
170 duration was slightly extended in posterior ectodermal cells by BIO treatment alone, but no
171 effect was observed in anterior ectodermal cells (Fig. S2F; wild-type: anterior 11.8±2.9
172 minutes, posterior 10.7±1 minutes and BIO: anterior 12.1±2.9 minutes, posterior 13.6±3.2
173 minutes). In the presence of nocodazole, however, (Fig. 4C) mitotic duration was significantly
174 shorter in anterior cells of the ventral ectoderm in BIO-treated embryos than in untreated
175 embryos (untreated: 66.4±19.1 minutes, BIO: 50.9±13.9 minutes), while no difference was
176 observed in posterior ventral ectodermal cells (untreated: 44.7±15.2 minutes, BIO: 43.1±11.3
177 minutes). Thus, SAC strength is specific to different cell populations. Our results also suggest
178 that GSK3 might be involved in enhancing SAC efficiency in anterior ectodermal cells. GSK3
179 activity as a SAC enhancing factor could be direct through phosphorylation of the SAC
180 machinery and/or the kinetochores to favor their interaction, or indirect through ß-catenin
181 mediated transcriptional control of SAC regulators. Although further work will be required to
182 distinguish between these possibilities, work carried out in mammalian cells showed that GSK3
183 promotes the recruitment of the SAC components Mad2, Bub1 and BubR1 to unattached
184 kinetochores and favors the formation of the inhibitory complex (Rashid et al., 2018),
185 supporting a direct role of GSK3 in increasing SAC strength.
186

187 **Material and Methods**
188

189 **Plasmids and RNAs**
190 The cDNA encoding Mad2-DN, a phosphomimic form of the human Mad2 that acts as
191 a dominant negative, was provided by Dr K. Wassmann (Wassmann et al., 2003a) and was
192 cloned into the plasmid pCS2 to allow RNA synthesis using SP6 RNA polymerase (mMessage-
193 mMachine kit, Invitrogen, Carlsbad, USA). Following in vitro transcription, a poly(A) tail was
194 added using a polyA-tailing kit (Invitrogen). The Mad2-DN RNA was injected into unfertilized
195 eggs at a concentration of 8 μg/μl.
196 Plasmids encoding NLS-3Venus, NLS-tomato, PH-tomato and PH-GFP were
197 previously described (McDougall et al., 2015). Following plasmid linearization with Sfi1,
198 RNAs were synthetized using T3 RNA polymerase (mMessage-mMachine kit, Invitrogen).
199 NLS-3Venus and NLS-tomato RNAs were injected in unfertilized eggs at the concentration of
200 4 μg/μl. PH-tomato and PH-GFP were injected in unfertilized eggs at a concentration of 1 μg/μl.

201 At these concentrations, these RNAs did not delay mitotic progression and had no effect on
202 embryonic development.
203 FoxA-a identified as Phmamm.g00001891 (Brozovic et al., 2018) was amplified from a cDNA
204 template using the primers: forward cgcTGTACAAGATGATGTTGTCGTCTCCC and reverse
205 cgcTGTACATTAGTTGGCCGGTACGCA. The FoxA-a coding sequence was used to replace the RFA
206 cassette in pSP72BSSPE-pFog::Venus-RFA provided by Patrick Lemaire (Roure et al., 2007) by
207 enzymatic digestion using BsrGI. The pFog>FoxA-a plasmid was injected at a concentration of 35
208 ng/μl.
209

210 **Gamete preparation**

211 Dissection of adult animals allowed collection of both sperm and eggs. Dry sperm was
212 kept at 4°C for a maximum of 3 weeks. Eggs were collected in microfiltered sea water (MFSW)
213 containing 5 mM TAPS ([tris(hydroxymethyl)methylamino]propanesulfonic acid), pH 8.2
214 (McDougall et al., 2015). The chorion was removed by treatment with 0.1% trypsin in 10 ml
215 MFSW-TAPS for 1.5-2 hours at room temperature (Sardet et al., 1989) . Dechorionated eggs
216 were washed in MFSW and kept at 18°C in MFSW with TAPS. Eggs were used within 36 hours
217 from collection. All glass- and plastic-ware for embryo handling was coated with 0.1% gelatin
218 and 0.1% formaldehyde (GF) (McDougall et al., 2015).
219 Prior to fertilization sperm was activated by incubating 9 μl of sperm (from 3 different
220 animals) in 1 ml of MFSW pH 9.2 for 30 minutes. Activated sperm was added to the eggs at a
221 ratio of approximately 10 μl of sperm to 5/20 eggs for small cultures or injected eggs, and 100
222 μl for 10 ml of MFSW for large cultures. Following fertilization eggs were transferred to a fresh
223 dish to remove excess sperm.
224

225 **Microinjection**

226 Microinjection of unfertilized eggs was carried out as previously described (Yasuo and
227 McDougall, 2018) with few changes. Briefly glass capillaries without filament (GC100 T10,
228 Harvard Apparatus) were used to store the RNA to be injected. Prior to loading, the RNA
229 solution was centrifuged at 13000 rpm at 10°C for 10 min to pellet impurities that could block
230 the needle. Capillaries were then filled sequentially with 2 μl of mineral oil, 0.5-1.5 μl RNA or
231 DNA solution and finally 1 μl of mineral oil and were kept at 4°C for several weeks. Needles
232 were made by pulling capillaries with a Narishige horizontal puller (PN-30).

233 Injections were performed using a Leica DM IL LED inverted microscope (10x
234 objective) in transmitted light. The needle was attached to a NarishigeIM300 injection box and
235 manipulated using a three-axis hydraulic micromanipulator (Narishige MMO-203 associated
236 with NarishigeNO-SIX-2 mounting adaptor and Narishige HI-7 pipette holder). Eggs were
237 immobilized in horizontal injection chambers (Yasuo and McDougall, 2018) filled with MFSW
238 and injected to 5% of their volume.
239

240 **Pole ablation**

241 Following fertilization, the cytoplasm of ascidian embryos undergoes significant
242 rearrangements that lead to the localization of many maternal factors into a transient surface
243 protrusion known as the contraction pole (Nishida, 1994; Nishida, 1996). Ablation of this pole
244 was performed by aspiration with a micropipette as previously described (Nishida, 1996). An
245 aspiration micropipette, formed by breaking the tip of a microinjection needle to obtain a blunt
246 opening, was connected to a mouth pipette. Eggs were fertilized in a petri dish and immediately
247 transferred into an injection chamber mounted on an inverted microscope as for microinjection.
248 The contraction pole was aspirated into the pipette by suction and a quick movement of the
249 needle perpendicularly to the egg surface sealed the membrane of the zygote. Eggs were then
250 transferred to a new dish to allow development.
251

252 **Drug treatments**

253 All drugs were stored in small aliquots at -20°C.
254 Nocodazole (Sigma-Aldrich, St. Louis, MO, USA) was resuspended in DMSO to obtain
255 a 33 mM stock solution and was used at a final concentration of 10 μM in MFSW. Reversine
256 (Axon Medchem, Groningen, The Netherlands) was resuspended in DMSO at 5 mM and used
257 at a final concentration of 0.5 μM in MFSW. Both drugs were added to MFSW when embryos
258 reached the analyzed stage and embryos were then maintained in the presence of the drug for
259 the duration of the experiment.
260 BIO ((2'Z,3'E)-6-Bromoindirubin-3'oxime, Millipore) was resuspended in DMSO to
261 obtain a 10 mM stock solution and was then used at a final concentration of 2.5 μM in MFSW.
262 Embryos were soaked in 2.5 μM BIO, in the dark, from the onset of gastrulation (stage 10,
263 about 5hpf). Two hours later (about 7 hpf) embryos were treated with 10μM nocodazole and
264 maintained in the presence of both drugs for the remaining of the experiment.
265

266 **Immunofluorescence**

267 For immunofluorescence, embryos were collected at the required stage and fixed
268 overnight in 100% methanol at -20°C. After fixation, embryos were washed 3 times in PBS
269 containing 0.1% triton-X-100 (PBST), then incubated in PBST containing 3% BSA (PBST-
270 BSA) for 1 hour at room temperature (RT) and finally incubated overnight at 4°C in PBST-
271 BSA with the anti-tubulin antibody, DM1A (mouse, Sigma-Aldrich) at 1:500 dilution. After
272 overnight incubation, excess antibody was removed by 3 consecutive washes in PBST.
273 Embryos were then incubated in PBST-BSA with either Alexa fluor 546 or Alexa fluor 488
274 anti-mouse secondary antibody (Jackson ImmunoResearch, Ely, UK; 1:2000) at RT for 1-2
275 hours. Following 2 further washes in PBST, embryos were incubated for 10 minutes in PBST
276 containing Hoechst 33342 (5 μg/ml), washed twice and then mounted in citifluor AF1 (Science
277 Services, München, Germany), for imaging with a Leica SP8 inverted confocal microscope
278 using a 40x objective.
279

280 **Time-Lapse Microscopy**

281 For live imaging, embryos were mounted between GF coated slide and coverslip, using
282 Dow Corning vacuum grease as spacer. In early stages (2- to 16-cell embryos) nuclei were
283 followed by brightfield microscopy while at later stages we relied on the localization of a
284 fluorescent protein, Venus or Tomato, fused to a nuclear localization signal (NLS-3Venus or
285 NLS-Tomato). The NLS protein accumulates in the nucleus during interphase, while from NEB
286 to NER (mitosis) the signal disperses in the cytoplasm. To distinguish individual cells within
287 the embryo, eggs were co-injected with an mRNA encoding the plasma-membrane marker PH-
288 GFP. Following fertilization embryos were maintained in MFSW until they reached the stage
289 of interest and then treated with the different drugs (nocodazole, reversine, BIO) or DMSO and
290 transferred to the appropriate microscope for recording. Live imaging was always performed in
291 a temperature-controlled room set at 19°C. When possible, control and treated embryos were
292 imaged in parallel on the same microscope.

293 Image acquisition was performed on the Plateforme d'Imagerie Microscopique de
294 Villefranche (PIM). For brightfield imaging, a z-stack covering the entire embryo with a z step
295 of 2 μm was acquired using a Zeiss (Oberkochen, Germany) Axiovert 100 or Axiovert 200
296 inverted microscope with bright field optics fitted with a 40x/1.1NA objective and equipped
297 with a CoolSnap Kino camera (Photometrics) and Metamorph acquisition software. Images
298 were acquired every 1-2 minutes. For NLS expressing embryos, a z-stack covering the entire

299 embryo with a z step of 2 μm was acquired using a Leica (Wetzlar, Germany) SP8 inverted
300 confocal microscope fitted with a 40x water immersion objective and 408, 488, and 552 nm
301 lasers and the Leica application suite acquisition software (LASX). Images were acquired every
302 2 minutes.
303

304 **Image analysis**

305 Images were analyzed using different softwares: Metamorph (Molecular Devices, San
306 Jose, USA), imageJ-Fiji (Schindelin et al., 2012), Imaris (Imaris, BitPlane, Zurich, Switzerland)
307 and Icy (de Chaumont et al., 2012) with the plugin Z-explorer developed by Christian Rouvière
308 at LBDV. Presence or absence of nuclei was determined manually by following each cell
309 overtime through the entire Z stack. At the 512-cell stage, when cells did not exit mitosis for
310 more than 1 hour before the end of acquisition, we assigned a mitotic duration of 60 minutes.
311 Approximate cell number was assessed by counting number of nuclei using the Spot tool in
312 Imaris. Cell volume was determined using the surface tool in Imaris: the cell contour was drawn
313 in each frame based on the signal from the plasma-membrane associated PH-GFP or PH-
314 Tomato, the reconstructed cell shape was confirmed using 3D visualization of the embryo and
315 then the cell volume was retrieved.
316

317 ***In situ* hybridization**

318 The sFRP1/5 identified as Phmamm.g0000599 (Brozovic et al., 2018) was amplified
319 from the clone AHC0AAA17YL13RM1. The FoxF identified as Phmamm.g07919 was
320 amplified from clone 64A02. After linearization by enzymatic digestion with SalI, an *in situ*
321 hybridization probe covering the coding sequence, was generated by in vitro transcription using
322 T7 RNA polymerase (Promega, Charbonnières-les-Bains, France) in presence of Digoxygenin-
323 labeled nucleotides (DIG RNA Labeling Mix, Roche, Bâle, Switzerland).

324 *In situ* hybridization experiments were performed as previously described with few
325 changes (Paix et al., 2009). Eggs and embryos were fixed overnight at 4°C in 4% formaldehyde,
326 100 mM MOPS, 0.5 M NaCl, pH 7.6, washed 3 times in PBS, progressively dehydrated in
327 ethanol (25%, 50%, 75%, 100%, 100%) and stored at −20°C. Fixed eggs and embryos were
328 then re-hydrated by addition of an equal volume of PBS/0.1% Tween 20 (PBSTw), washed
329 once in PBSTw and then incubated with 2 µg/ml proteinase K in PBSTw for 25 minutes at
330 room temperature (RT). After 3 washes in PBSTw, embryos were fixed again in PBS containing
331 4% formaldehyde (1 h, RT) and washed again to remove formaldehyde. Embryos were then

332 incubated in hybridization buffer (50% formamide, 6× saline sodium citrate (SSC), 5×
333 Denhardt's solution, 1 mg/ml yeast RNA, 0.1% Tween, pH = 6.5/7.5) for 1 h at 65 °C. Probes
334 were added to fresh hybridizations solution at a final concentration of 0.5 ng/µl and
335 hybridization was performed overnight at 65°C. After hybridization, embryos were washed at
336 65°C twice in 50% formamide, 5× SSC, 1% SDS (30 min), twice in 50% formamide, 2× SSC,
337 1% SDS (15 min), once in 2× SSC, 0.1% Tween (15 min) and twice in 0.2× SSC, 0.1% Tween
338 (15 min). All solutions were at pH 6.5/7.5. Embryos were then incubated in blocking buffer
339 (0.15 M NaCl, 0.5% BBR, 0.1M Tris pH8) for 1h at RT. Anti-DIG AP antibody (Roche,
340 1:4000) was added in fresh blocking solution and incubated at 4 °C overnight. After incubation,
341 embryos were washed 5 times in PBSTw (3*10 min, 30 min, 1 h) and then in TBSTw at 4°C
342 overnight. Embryos were washed once with reaction buffer (0.1 M Tris pH 9.5, 50 mM $MgCl_2$,
343 0.1M NaCl, 0.1% Tween) and then the detection reaction was carried out in a buffer containing
344 3.5 µl/ml of of nitro blue tetrazolium (NBT) and 5-bromo-4-chloro-3-indolyl-phosphate (BCIP)
345 (Roche, Bâle, Switzerland). The reaction was stopped with 0.05 M EDTA in PBS and embryos
346 were washed in PBSTw. Embryos were fixed in 4% formaldehyde in PBS, washed and mounted
347 in 80% Glycerol. *In situ* hybridization experiments were imaged using an optical microscope
348 (Zeiss Imager A2) with a 20x objective.
349

350 **Quantification and statistical analysis**

351 Number of analyzed embryos (N) and cells (n) are reported under each graph. For each
352 experiment at least 3 independent biological repeats were included. For statistical analysis the
353 non-parametric test of Wilcoxon-Mann-Whitney was applied. For all comparisons, we used
354 population medians as the mean can be affected by extreme values and is highly impacted by
355 outliers (Gaddis and Gaddis, 1990). However, means and standard deviations are also provided
356 in the text. Statistical tests and graphics were performed using the R software (R Core Team,
357 2016) and the library "pretty R" (Grosjean and Lemon, 2015) was used to retrieve median,
358 mean and standard deviation.

359 Box plot represents the distribution of the data using quartiles (Q). Q1, Q2 and Q3 being
360 respectively the values below which lie 25%, 50% and 75% of the data points. Q1 and Q3 form
361 the limits of the box and the median Q2 is indicated by a bolder line. The whiskers represent
362 the range in which most values are found, whereas the values outside represent the outliers.
363

Acknowledgments

We are grateful to E. Houliston, H. Yasuo, C. Hudson, S. Darras, R. Dumollard, P. Lemaire and K. Wassmann for discussion, sharing of reagents or critical reading of the manuscript. We would also like to thank C. Hebras, F. Bekkouche, L. Gilletta, M. Temagoult, S. Benaicha, and S. Schaub for technical assistance. We thank the Service Aquarologie of CRB (IMEV-FR3761) for access to marine facilities and animals. This service is supported by EMBRC-France, whose French state funds are managed by the ANR within the investments for the future program under reference ANR-10-INSB-02.

This research was funded by the CNRS and from PACA region (project Mepanep, 2014_03738).

Author contributions

Conceptualization, S.C. and J.C.; Methodology, S.C., J.C. and A.M.; Investigation, M.R., L.B., A.M., J.C. and S.C.; Writing-Original draft, S.C. and J.C.; Funding Acquisition; S.C.; Resources, A.M. and S.C.; Supervision; E.C., J.C and S.C.

Declaration of interests

The authors declare no competing interests.

References

Brozovic, M., Dantec, C., Dardaillon, J., Dauga, D., Faure, E., Gineste, M., Louis, A., Naville, M., Nitta, K. R., Piette, J., et al. (2018). ANISEED 2017: extending the integrated ascidian database to the exploration and evolutionary comparison of genome-scale datasets. *Nucleic Acids Res*. 46, D718–D725.

Chenevert, J., Roca, M., Besnardeau, L., Ruggiero, A., Nabi, D., McDougall, A., Copley, R. R., Christians, E. and Castagnetti, S. (2020). The Spindle Assembly Checkpoint Functions during Early Development in Non-Chordate Embryos. *Cells* 9,.

Chunduri, N. K. and Storchová, Z. (2019). The diverse consequences of aneuploidy. *Nat. Cell Biol*. 21, 54–62.

de Chaumont, F., Dallongeville, S., Chenouard, N., Hervé, N., Pop, S., Provoost, T., Meas-Yedid, V., Pankajakshan, P., Lecomte, T., Le Montagner, Y., et al. (2012). Icy: an open bioimage informatics platform for extended reproducible research. *Nat. Methods* 9, 690–696.

Dumollard, R., Minc, N., Salez, G., Aicha, S. B., Bekkouche, F., Hebras, C., Besnardeau, L. and McDougall, A. (2017). The invariant cleavage pattern displayed by ascidian

398 embryos depends on spindle positioning along the cell's longest axis in the apical
399 plane and relies on asynchronous cell divisions. *eLife* 6, e19290.

400 Encalada, S. E., Willis, J., Lyczak, R. and Bowerman, B. (2005). A Spindle Checkpoint
401 Functions during Mitosis in the Early Caenorhabditis elegans Embryo. *Mol. Biol. Cell*
402 16, 1056–1070.

403 Feinberg, S., Roure, A., Piron, J. and Darras, S. (2019). Antero-posterior ectoderm patterning
404 by canonical Wnt signaling during ascidian development. *PLOS Genet.* 15, e1008054.

405 Gaddis, G. M. and Gaddis, M. L. (1990). Introduction to biostatistics: Part 2, Descriptive
406 statistics. *Ann. Emerg. Med.* 19, 309–315.

407 Galli, M. and Morgan, D. O. (2016). Cell size determines the strength of the spindle assembly
408 checkpoint during embryonic development. *Dev. Cell* 36, 344–352.

409 Gerhold, A. R., Poupart, V., Labbé, J.-C. and Maddox, P. S. (2018). Spindle assembly
410 checkpoint strength is linked to cell fate in the Caenorhabditis elegans embryo. *Mol.*
411 *Biol. Cell* 29, 1435–1448.

412 Grosjean, P. and Lemon (2015). prettyR: Pretty Descriptive Stats.

413 Jia, L., Kim, S. and Yu, H. (2013). Tracking spindle checkpoint signals from kinetochores to
414 APC/C. *Trends Biochem. Sci.* 38, 302–311.

415 Kyogoku, H. and Kitajima, T. S. (2017). Large Cytoplasm Is Linked to the Error-Prone
416 Nature of Oocytes. *Dev. Cell* 41, 287-298.e4.

417 Lamy, C., Rothbächer, U., Caillol, D. and Lemaire, P. (2006). Ci-FoxA-a is the earliest
418 zygotic determinant of the ascidian anterior ectoderm and directly activates Ci-
419 sFRP1/5. *Development* 133, 2835–2844.

420 Lane, S. I. R., Morgan, S. L., Wu, T., Collins, J. K., Merriman, J. A., ElInati, E., Turner, J. M.
421 and Jones, K. T. (2017). DNA damage induces a kinetochore-based ATM/ATR-
422 independent SAC arrest unique to the first meiotic division in mouse oocytes. *Dev.*
423 *Camb. Engl.* 144, 3475–3486.

424 McDougall, A., Chenevert, J., Pruliere, G., Costache, V., Hebras, C., Salez, G. and
425 Dumollard, R. (2015). Chapter 17 - Centrosomes and spindles in ascidian embryos
426 and eggs. In *Methods Cell Biol.* (ed. Basto, R.) and Oegema, K.), pp. 317–339.
427 Academic Press.

428 Minshull, J., Sun, H., Tonks, N. K. and Murray, A. W. (1994). A MAP kinase-dependent
429 spindle assembly checkpoint in Xenopus egg extracts. *Cell* 79, 475–486.

430 Musacchio, A. and Salmon, E. D. (2007). The spindle-assembly checkpoint in space and time.
431 *Nat. Rev. Mol. Cell Biol.* 8, 379–393.

432 Nishida, H. (1994). Localization of determinants for formation of the anterior-posterior axis
433 in eggs of the ascidian Halocynthia roretzi. *Development* 120, 3093–3104.

434 Nishida, H. (1996). Vegetal egg cytoplasm promotes gastrulation and is responsible for
435 specification of vegetal blastomeres in embryos of the ascidian Halocynthia roretzi.
436 *Development* 122, 1271–1279.

437 Nishikata, T., Hibino, T. and Nishida, H. (1999). The centrosome-attracting body,
438 microtubule system, and posterior egg cytoplasm are involved in positioning of
439 cleavage planes in the ascidian embryo. *Dev. Biol.* 209, 72–85.

440 Paix, A., Yamada, L., Dru, P., Lecordier, H., Pruliere, G., Chenevert, J., Satoh, N. and Sardet,
441 C. (2009). Cortical anchorages and cell type segregations of maternal
442 postplasmic/PEM RNAs in ascidians. *Dev. Biol.* 336, 96–111.

443 R Core Team, R. C. T. (2016). R: A Language and Environment for Statistical Computing.

444 Rashid, M. S., Mazur, T., Ji, W., Liu, S. T. and Taylor, W. R. (2018). Analysis of the role of
445 GSK3 in the mitotic checkpoint. *Sci. Rep.* 8,.

446 Roure, A., Rothbächer, U., Robin, F., Kalmar, E., Ferone, G., Lamy, C., Missero, C., Mueller,
447 F. and Lemaire, P. (2007). A Multicassette Gateway Vector Set for High Throughput
448 and Comparative Analyses in Ciona and Vertebrate Embryos. *PLoS ONE* 2,.

449 Santaguida, S., Tighe, A., D'Alise, A. M., Taylor, S. S. and Musacchio, A. (2010). Dissecting
450 the role of MPS1 in chromosome biorientation and the spindle checkpoint through the
451 small molecule inhibitor reversine. *J. Cell Biol.* 190, 73–87.

452 Sardet, C., Speksnijder, J., Inoue, S. and Jaffe, L. (1989). Fertilization and ooplasmic
453 movements in the ascidian egg. *Dev. Camb. Engl.* 105, 237–249.

454 Schindelin, J., Arganda-Carreras, I., Frise, E., Kaynig, V., Longair, M., Pietzsch, T.,
455 Preibisch, S., Rueden, C., Saalfeld, S., Schmid, B., et al. (2012). Fiji: an open-source
456 platform for biological-image analysis. *Nat. Methods* 9, 676–682.

457 Vázquez-Diez, C., Paim, L. M. G. and FitzHarris, G. (2019). Cell-Size-Independent Spindle
458 Checkpoint Failure Underlies Chromosome Segregation Error in Mouse Embryos.
459 *Curr. Biol.* 29, 865-873.e3.

460 Wassmann, K., Liberal, V. and Benezra, R. (2003a). Mad2 phosphorylation regulates its
461 association with Mad1 and the APC/C. *EMBO J.* 22, 797–806.

462 Wassmann, K., Niault, T. and Maro, B. (2003b). Metaphase I arrest upon activation of the
463 Mad2-dependent spindle checkpoint in mouse oocytes. *Curr. Biol. CB* 13, 1596–1608.

464 Yasuo, H. and McDougall, A. (2018). Practical Guide for Ascidian Microinjection: Phallusia
465 mammillata. *Adv. Exp. Med. Biol.* 1029, 15–24.

466

467
468
469

470 **Figures**

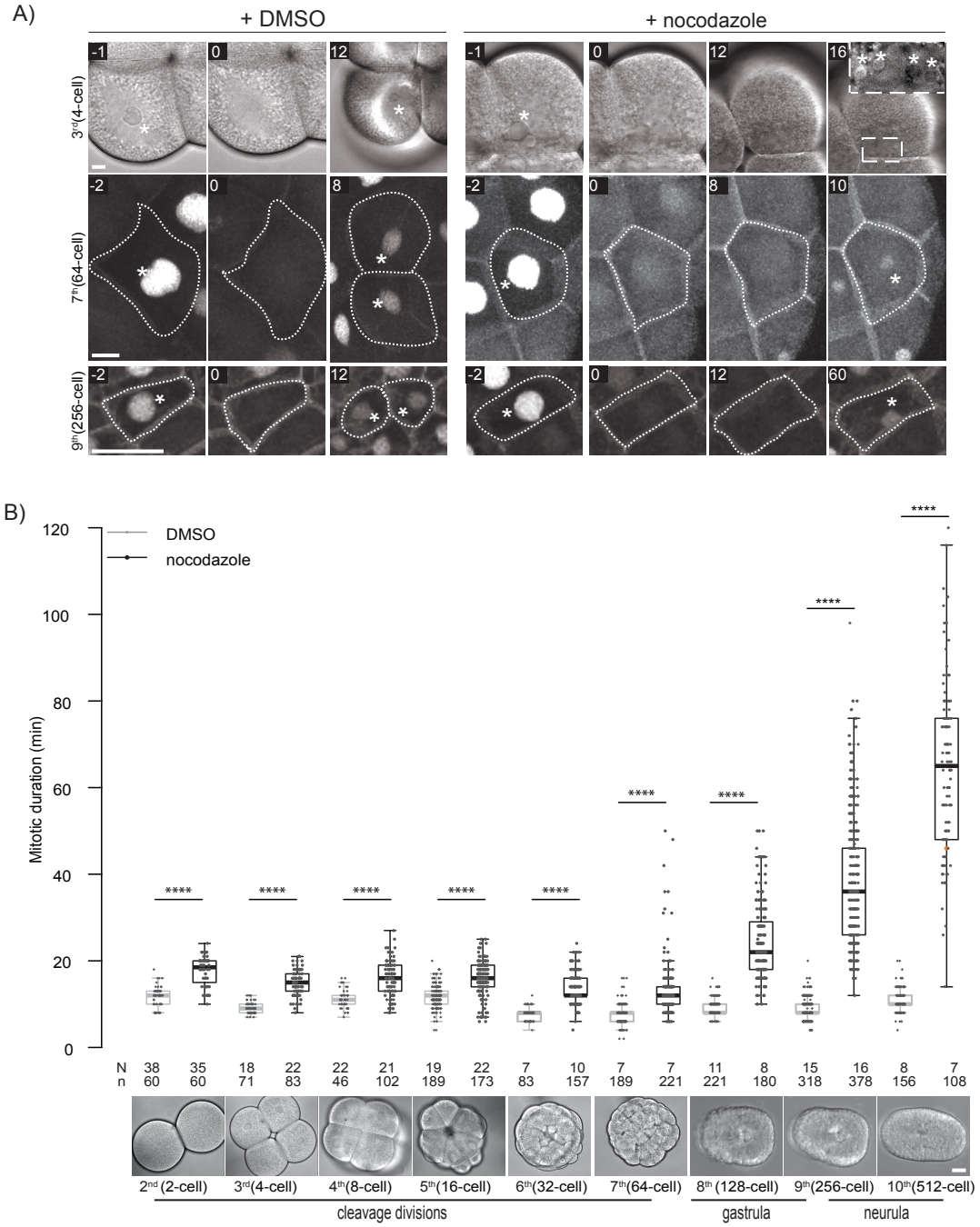

471
472 **Figure 1: Nocodazole treatment induces a prolonged delay in mitotic progression from**
473 **the 8th cell cycle.**

A) Representative images of 4- (top), 64- (middle) and 256-cell (bottom) embryos treated with DMSO (left) or with 10 μM nocodazole (right). Asterisks indicate nuclei. NEB is considered as time 0 and time before or after NEB (minutes) is indicated on each image. For early stages (2-16 cell) nuclei were visualized by brightfield video microscopy. See also Movie 1. For later stages (32-512 cell), nuclei were visualized with the fluorescent label NLS-3xVenus and plasma membrane with PH domain-GFP; see also Movie 2. Dotted lines indicate cell periphery. Fluorescence images are projections of the confocal Z stack covering the whole cell. **B)** Quantification of mitotic duration in DMSO (light grey) or nocodazole (dark grey) treated embryos from 2nd to 10th cell cycle (2- to 512-cell). Representative brightfield images of *P. mammillata* embryos are presented below the plot for all analyzed stages. Nocodazole was added as soon as embryos reached the analyzed stage. Each dot represents a cell. Boxes represent 25-75th percentiles, and the median is shown. Number of analyzed embryos (N) and cells (n) is given for each stage. Test of Wilcoxon-Mann-Whitney performed using all cells: non-significant (ns), p-value ≤ 0.05 (*), ≤ 0.01 (**), ≤ 0.001 (***), ≤ 0.0001 (****). Scale bars are 10 μm in A and 30 μm in B.

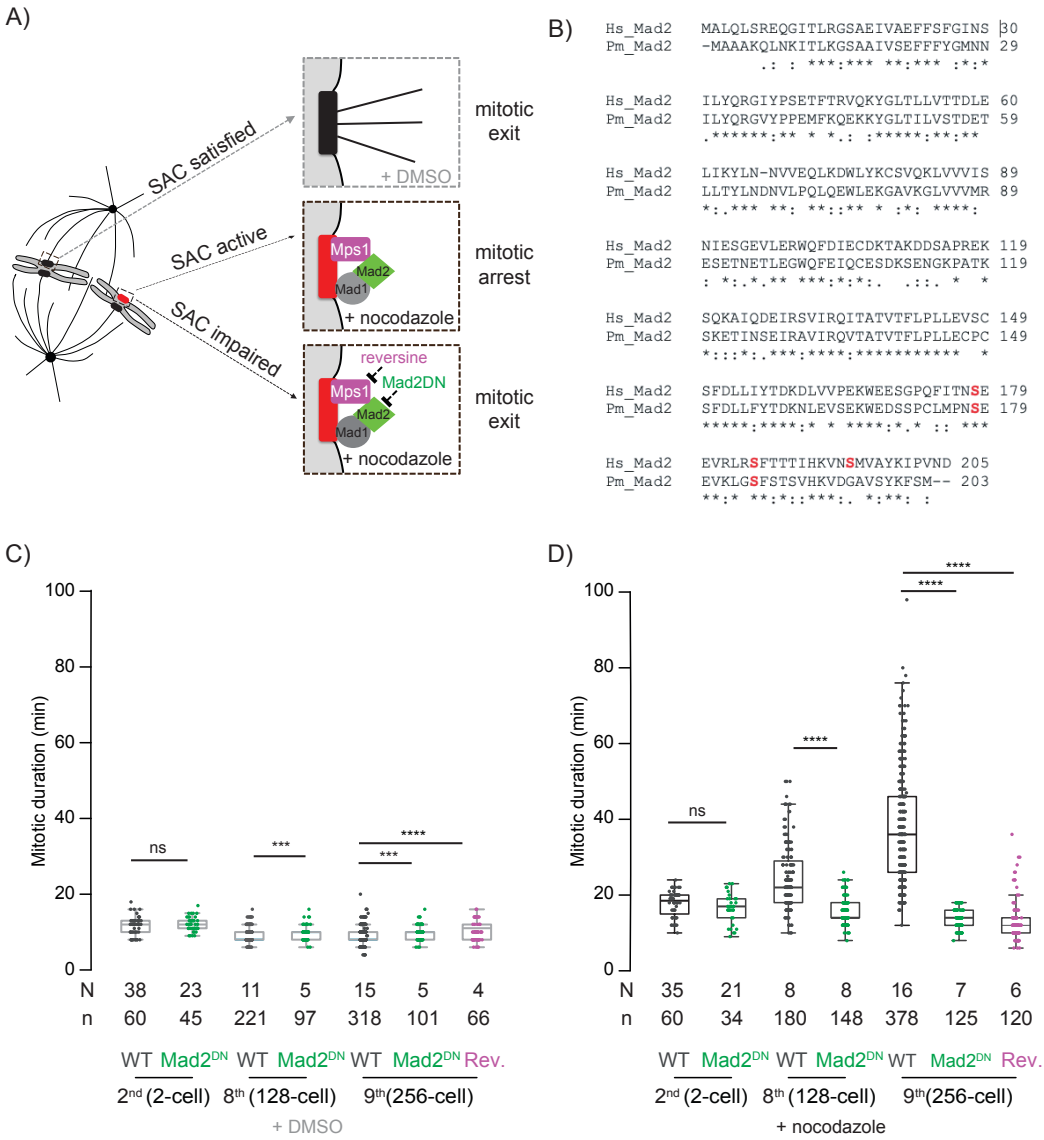

Figure 2: SAC activity is acquired at the 8th cell cycle.

A) Schematic representation of mitotic chromosomes and their association with spindle microtubules (top). SAC proteins, Mps1, Mad1 and Mad2 localize to an unattached kinetochore, leading to SAC activation and inhibition of APC/C activity (middle). Treatment with the Mps1 inhibitor, reversine, or overexpression of Mad2-DN impairs SAC activity resulting in premature mitotic exit (bottom). **B)** Alignment of Mad2 sequence from human and *P. mammillata*. The serine residues mutated in the Mad2-DN construct are indicated in red. **C)** Quantification of mitotic duration in DMSO and **D)** in nocodazole treated embryos at 2-, 128- and 256-cell stage in wild-type embryos (black) or following SAC impairment by either overexpression of Mad2-DN (green) or treatment with reversine (magenta). Drugs (nocodazole

502 and reversine) were added when embryos reached the analyzed stage. Boxes are as in Figure
503 1B. See also Movie 3 and 4.

504

505

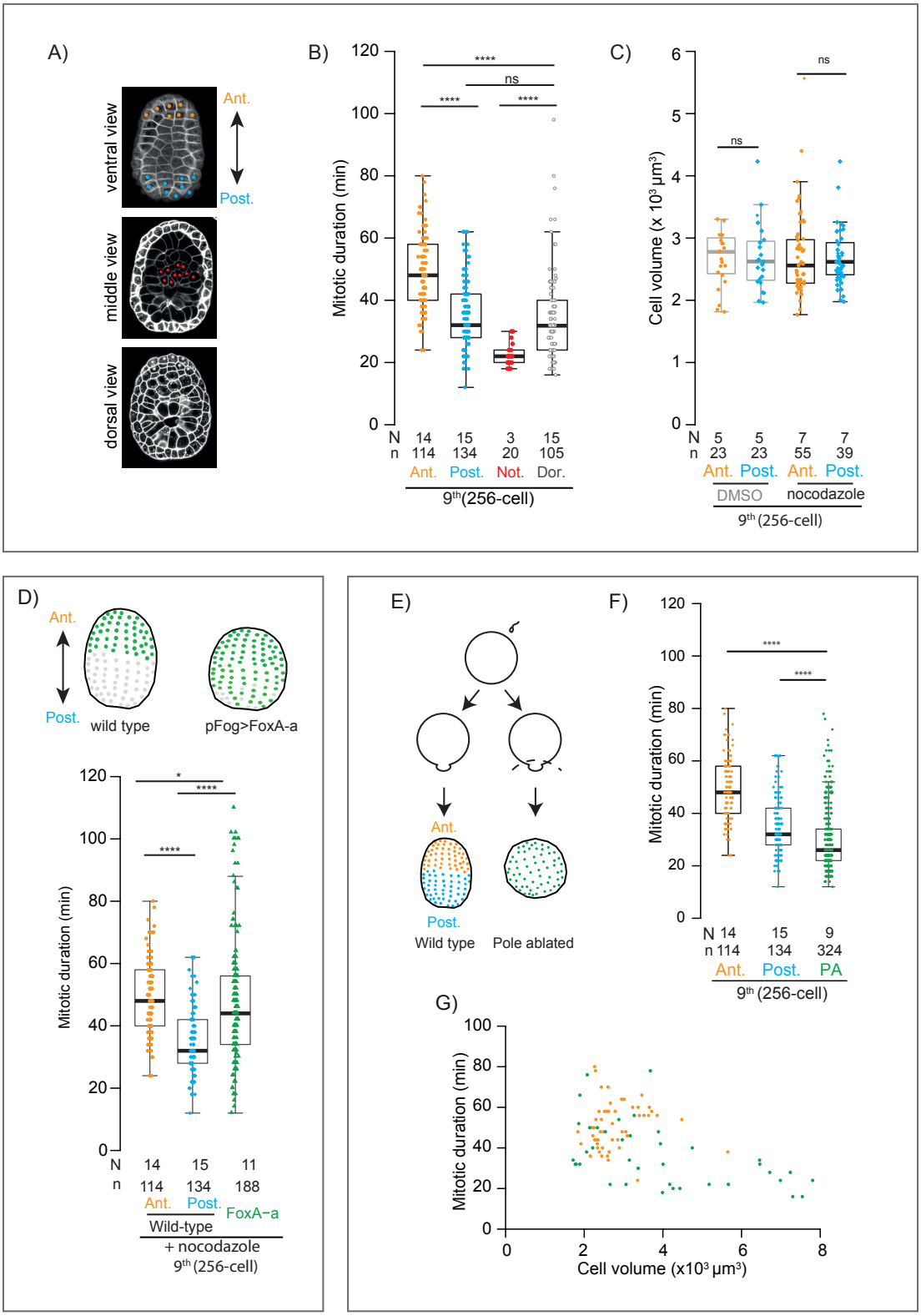

Figure 3: SAC efficiency is stronger in anterior ectodermal cells.

508 **A**) Ventral, middle and dorsal views of cell mask stained 256-cell stage embryo, indicating
509 areas where mitotic duration was analyzed for anterior and posterior ectodermal cells: ventral
510 anterior (orange) and posterior (blue) ectoderm, notochord (red) and dorsal ectoderm (grey). **B)**
511 Mitotic duration in ventral anterior ectoderm (orange), ventral posterior ectoderm (blue),
512 notochord (red) and dorsal cells (grey) of nocodazole treated wild type 256-cell stage embryos.
513 **C)** Cell volume of ventral anterior (orange) and posterior (blue) ectodermal cells in 256-cell
514 stage embryos in the presence of either DMSO (grey) or nocodazole (black). **D)** Top: schematic
515 representation of FoxA-a expression in wild type and pFog>FoxA-a over-expressing embryos.
516 Green circles represent FoxA-a expressing nuclei. Bottom: mitotic duration in ventral anterior
517 ectoderm (orange), ventral posterior ectoderm (blue) and pFog>FoxA-a overexpressing
518 embryos (green) at the 9th cell cycle in the presence of nocodazole. **E)** Schematic representation
519 of non-manipulated (left) and pole-ablated (right) fertilized eggs and resultant embryos. **F)**
520 Mitotic duration in the presence of nocodazole for wild type ventral anterior (orange) and
521 posterior (blue) ectodermal cells and cells from pole-ablated embryos (green) at the 9th cell
522 cycle. **G)** Mitotic duration in pole-ablated embryos and anterior ectodermal cells treated with
523 nocodazole as a function of cell volume at the 9th cell cycle. For B), C), D) and F) boxes are as
524 in Figure 1B. See also Figure S2. Scale bar is 30μm.
525
526

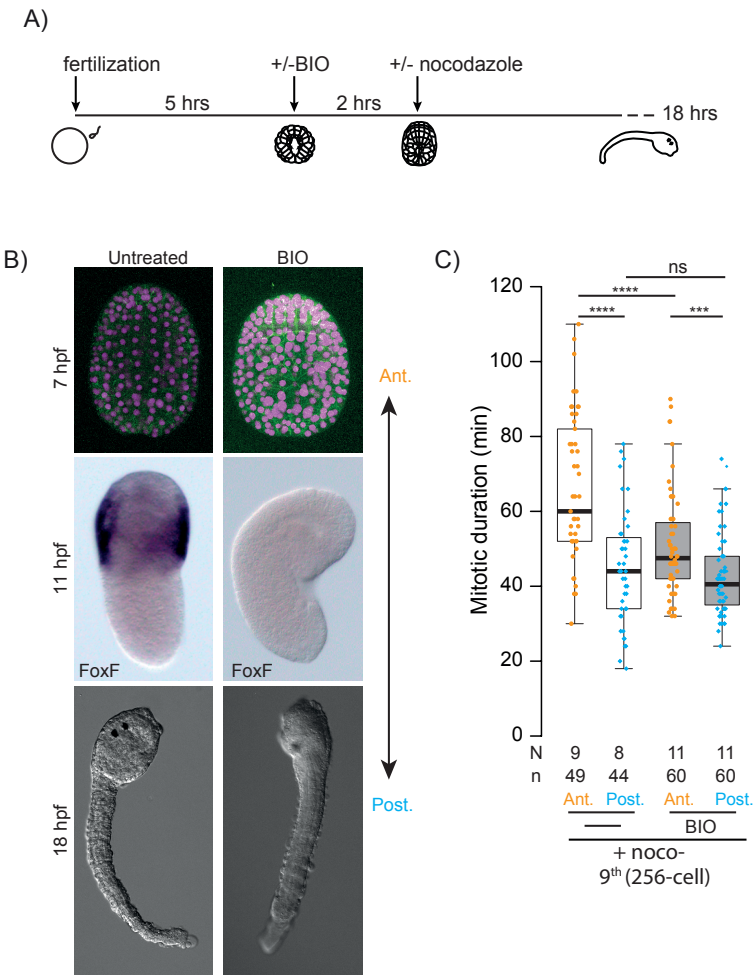

Figure 4: GSK3 enhances SAC activity in anterior ectodermal cells.

A) Schematic representation of test used to analyze impact of GSK3 activity on mitotic duration. **B)** Representative images of control (left) and BIO-treated (right) 256-cell stage embryos (7 hpf), expressing NLS-Tomato (magenta) and PH-GFP (green), late neurula embryos showing the expression pattern of the anterior marker FoxF (11 hpf) and tadpoles (18 hpf). **C)** Mitotic duration in ventral anterior (orange) and posterior (blue) ectodermal cells of control (DMSO) embryos and BIO-treated embryos at the 9th cell cycle in the presence of nocodazole. Box plot in C is as in Figure 1B. Scale bar is 30μm.